47th AIAA Aerospace Sciences Meeting Including The New Horizons Forum and Aerospace Exposition
5 - 8 January 2009, Orlando, Florida

AIAA 2007-0940

Numerical Simulation of Hypersonic Boundary Layer Receptivity and Stability on Blunt Circular Cones

Xiaolin Zhong[1]
University of California, Los Angeles, California 90095

Abstract

For hypersonic boundary layers over blunt cones, the transition reversal phenomenon refers to the experimental observation that the laminar-turbulent transition location moves upstream with increasing nose radius when it is larger than a certain critical value. Currently, there is no satisfactory explanation for transition reversal phenomenon. All previous linear stability theory (LST) and numerical simulation studies on the nose bluntness effects have not found transition reversal. The previous theoretical and computational studies, however, have not been done on the actual experimental flow conditions which had shown transition reversal. The most extensive experimental results on transition reversal are those reported by Stetson for the case of Mach 5.5 flow over blunt cones. The objective of this paper is to conduct numerical simulation studies of Stetson's Mach 5.5 experiments on the nose bluntness effects. The results of both steady and unsteady flow simulations are presented. Three nose radii of 0.0156in, 0.5in, and 1.5in are used to study the nose bluntness effects on boundary layer instability and transition. The simulation results show that the increase of nose bluntness leads to the substantial decrease in local Reynolds numbers along the edge of the boundary layers. The unsteady results are compared with those of LST reported in a companion paper by Lei and Zhong (AIAA-2009-0943).

1 Introduction

The accurate prediction of laminar-turbulent transition in hypersonic boundary layers is a critical part of the aerodynamic heating analyses on hypersonic vehicles. Since 1950s, extensive wind-tunnel and flight-test experiments on boundary layer transition and a number of stability experiments have been conducted for hypersonic flows over circular cones [1, 2]. Schneider [1, 2] did an extensive review of the existing literature on these experiments for both flight test and wind tunnel experiments. Though many of these experiments did not measure transition mechanisms and were carried out in noisy wind tunnels, the experimental studies have led to better understanding of the effects on transition of many parameters, including nose bluntness, Mach number, freestream noise, surface and stagnation temperatures, freestream unit Reynolds numbers, cone half angles, angles of attack, and surface roughness, etc. Nevertheless, so far, the effects of many of these parameters on transition are still not well understood.

One of the unexplained phenomena is the transition reversal phenomenon as the nose bluntness of the cones increase [3, 4]. The transition reversal phenomenon refers to the experimental observation that the transition location moves downstream when the nose radius is increased. This trend is, however, reversed when the nose radius is larger than a certain critical value. Increasing nose radius after that will lead to a forward movement of the transition location. The downstream movement of the transition location at small radii can be explained by the reduction of local Reynolds numbers owing to the entropy layer created by the nose bluntness. However, there is still no satisfactory explanation for the cause of transition reversal at large nose bluntness. There is also a possibility that the surface roughness and freestream noise in wind tunnel play a role in the reversal.

[1]Professor, Mechanical and Aerospace Engineering Department, Associate Fellow, AIAA.

Most of the previous theoretical and computational studies of the transition reversal have been on the Stetson *et al.'s*[5, 6] stability experiments on an axisymmetric blunt cone in a Mach 7.99 freestream. The half angle of the cone was 7°, the nose radii were 1.5 inches and larger, and the freestream Reynolds number based on the nose radius was 33,449. The Reynolds number based on the total length of the cone was about 9 millions. Detailed fluctuation spectra of the disturbance waves developing along the body surface were measured in the experiments. It was found that the disturbances in the boundary layer were dominated by the second mode instability. Significant super harmonic components of the second modes were observed after the second mode became dominant. Compared with similar hypersonic flow over a sharp cone, the second mode instability of the blunt cone appeared in much further downstream locations. This indicates a stabilization of the boundary layer by slight nose bluntness. Stability experiments of hypersonic flows over sharp or blunt cones have also been carried out by other researchers. Demetriades[7, 8] did extensive stability experiments on hypersonic boundary layers over axisymmetric cones. Recently, Maslov and his colleagues[9, 10] reported their stability experiments on supersonic and hypersonic flows over sharp or blunt cones.

The normal-mode linear stability characteristics of the boundary-layer flow over the same blunt cone as Stetson *et al.*'s experiments have been studied by a number of researchers[11-14]. Malik *et al.* [11] computed the neutral stability curve and compared the growth rates obtained by LST with the experimental results. The steady base flow solution was computed by using the parabolized Navier-Stokes equations. They found that the nose bluntness stabilizes the boundary layer. The growth rates predicted by the LST were compared with Stetson *et al.*'s experimental results at the surface location of $s = 175$ nose radii (0.667 m). The linear stability analyses predicted slightly lower frequency for the dominant second mode, but much higher amplification rates than the experimental results. Rosenboom et al.[15] did further study on the effect of nose bluntness on the linear stability of hypersonic flow over Stetson's blunt cone. In their studies, the cone geometry and freestream conditions were adapted to the Stetson's experiments. Three cases of blunt cones of different nose radii, which cover both ``small" and ``large'' bluntness, were considered. The purpose was to investigate, by linear stability analysis, the transition reversal phenomenon observed in experiments at ``large" bluntness[4, 16]. By a linear stability analysis, Rosenboom et al. confirmed a monotonic downstream movement of the second mode critical Reynolds number as nose radius increases. However, their linear stability analysis still cannot explain the transition reversal phenomena observed in experiments at ``large" bluntness.

Zhong et al.[17-19] have conducted numerical simulation of the stability and receptivity of Stetson's Mach 8 flow over blunt cones. In [18], the numerical results for the steady base flow were compared with the experimental results of Stetson et al.[5], and with the numerical results of Esfahanian[20]. In addition, a normal-mode linear stability analysis was used to identify the main components of boundary-layer disturbances generated by forcing freestream fast acoustic waves. It was found that neither the first mode nor the second mode instability waves are excited directly by freestream fast acoustic waves in the early region along the cone surface, although the Mack modes can be unstable there. Instead, the second mode is excited downstream of the second-mode Branch I neutral stability point. The delay of the second-mode excitation is a result of the fact that the hypersonic boundary-layer receptivity is governed by a two-step resonant interaction process: 1) resonant interactions between the forcing waves and a stable boundary-layer wave mode I near the leading edge region, and 2) resonant interactions between the induced stable mode I and the unstable second Mack mode downstream.

The current work is motivated by our previous numerical simulation study [19] of the effect of nose bluntness on hypersonic boundary layer receptivity over a blunt cone. In [19], we conducted a numerical study on the effects of nose bluntness on the receptivity to free-stream acoustic waves for hypersonic flow by comparing the results of three nose radii. The flow conditions duplicated the experiments of Stetson et al. [5] and investigated the effects of nose bluntness on receptivity. Three nose radii were chosen to be the same as those used in Rosenboom et al.'s stability analysis. They are 3.81 mm (Case A), 17.78mm (Case B), and 42.67mm (Case C). The first nose radius belonged to category of ``small" nose bluntness, while the second and third cases fell into the region of ``large" bluntness. By using the numerical simulation, the initial receptivity process was computed accurately. The effects of bow shock interaction with forcing waves, the effects of the entropy layer and non-parallel boundary layer are also taken into account in the numerical simulation. A total of 15 frequencies are computed in the receptivity simulation for each case. It is found that, in those three test cases, the basic receptivity mechanism of hypersonic flow over the blunt cone with different nose radii is essentially the same. Specifically, the receptivity is a result of the resonant interactions between forcing waves and boundary-layer wave modes near the nose region, and the resonant interactions between different boundary-layer wave modes downstream. As the nose radius increases from ``small"

to ``large'', the results in [5] showed no reversal in the location of instability wave induced by the receptivity process. In other words, the location of initial excitation of the second instability mode always moved downstream as the nose bluntness was increased.

Therefore, currently, the small bluntness effects of transition delay can be explained by the reduction of local Reynolds numbers. However, the mechanisms of transition reversal are not clear for the larger bluntness effects. The possible explanation for the experimental observation of transition reversal can be the instability of entropy layers, the surface roughness effects, wind tunnel noise in conventional noise tunnel, etc. So far, LST and computational studies have been done only on the test cases of Stetson's Mach 8 experiments [5]. All previous calculations have found no instability reversal at very large nose radii. On the other hand, Stetson's Mach 8 test model was not long enough to observe transition in his experiments. In other words, transition reversal phenomenon was not actually observed experimentally in Stetson's Mach 8 test cases. It is worthwhile to study, by both numerical simulation and LST, the mechanisms of transition reversal on the actual experimental conditions which have showed transition reversal.

Though the delay of transition by slight nose blunting has been found by many experiments since 1950s, the transition reversal at large nose bluntness has only been reported by a few researchers. Stetson et al. [3, 21] were the first ones to report concrete results on transition reversal. The only other reversal results were shown in Figure 3 of a paper by Ericsson [4], who cited an unpublished reported by Softley [22]. Many wind tunnel and flight tests have also been conducted on hypersonic boundary layer transition over blunt circular cones [1, 2]. Examples of these experiments are shown in *Table 1* [3, 5, 9, 10, 21, 23-30]. The freestream Mach numbers of these cases range from 3 to 8, while the cone half angles have a range of 5 to 9.75 degrees. There is a wide range of freestream unit Reynolds numbers. The effects of the nose bluntness, Mach number and unit Reynolds numbers were studied. Most of these experiments were conducted in conventional noisy wind tunnels where the effects of tunnel noise can have significant on the transition. With the exception of Stetion's 1984 experiments [31] and Maslov's 2001 experiments [9, 10], most of these experiments have not been studied by direct numerical simulation or by linear stability analysis. No systematic transition reversal results have been reported in these papers except Stetson's test cases.

Therefore, the most extensive experimental results on transition reversal are those reported by Stetson especially the case of Mach 5.5 flow over sharp and blunt cones [3]. *Figure* 1 shows a schematic of Stetson's test models with ten nose radii: $\frac{1}{32}, \frac{1}{16}, \frac{3}{32}, \frac{1}{8}, \frac{5}{32}, \frac{6}{32}, \frac{7}{32}, \frac{1}{4}, \frac{1}{2},$ and $1\frac{1}{2} in$. The model was polished such that the general surface finish is approximately 10 μin and it can be considered to be smooth surface. Transition reversal was observed in these test models as shown in Figure 2, which shows the transitional Reynolds numbers vs. nose radius Reynolds numbers, which are based on freestream flow conditions. This figure is created by using Stetson's experimental results tabulated in Table 2 of [3]. The figure shows a clear transition reversal as Re_n increases, with the Re_n of 2×10^5 serving as the dividing line between "large" and "small" nose radii. This results are very similar to the results in [4] for freestream Mach number of 10 or higher.

So far, there has not been any LST or DNS study on the Stetson's Mach 5.5 cases, which are one of the very few experimental test cases actually showing transition reversal. It will be valuable if these experiments can be systematically re-analyzed by modern DNS and linear stability techniques to study the effects on transition by nose bluntness. The experimental results on the parametric effects on transition can be compared with the computations. Therefore, the objectives of this paper and a companion paper [32] are to conduct the LST and DNS studies of the cases of Stetson's Mach 5.5 experiments on the nose bluntness effects. In this paper, we present both steady and unsteady solutions of three test cases of different nose radii: $\frac{5}{32}, \frac{1}{2},$ and $1\frac{1}{2} in$. All other flow conditions are the same for these cases. The freestream unit Reynolds number is chosen to be the same as the actual experimental cases shown in Table 2 of [3].

We have developed a fifth-order shock-fitting code to compute the Navier-Stokes equations for such flows [33]. The code has been used to study the study and unsteady hypersonic flow over a 7 degree blunt cone of Stetson's 1984 experiments [18, 19]. The use of high-order shock fitting schemes makes it possible to obtain highly steady

and unsteady accurate solution of hypersonic flow over the cones with entropy layer effects. The steady mean flows can be used as a starting point for both the linear stability calculations of the same flow and the numerical simulation of freestream receptivity and stability of the boundary layers. By using the numerical simulation of the shock-fitting approach, the initial receptivity process can be computed accurately in the current study. The effects of bow shock interaction with forcing waves, the effects of the entropy layer and non-parallel boundary layer are also taken into account in the numerical simulation. We will compute mean flows for those test cases first. Subsequently, we will conduct parameters studies on the receptivity and stability on those test cases.

These calculations will also generate high-quality numerical solutions for the experimental flow fields for analytical analysis, e^n prediction of transition and linear stability calculations. In a separate paper [32], the steady flow solutions obtained in this paper are used to conduct LST calculations on the transition reversal effects. This paper reports our work in progress. More extensive steady and unsteady results of other nose radii and flow conditions and other test cases shown in *Table 1* will be reported in future papers.

Table 1. Summary of Wind-Tunnel and Flight Test Cases for Blunt Circular Cones.

Case No.	**Researchers and Citations**	M_∞	$\mathrm{Re}_\infty \times 10^{-6} / ft$	T_0 **(R)**	**Nose radius (in)**	**half angle (deg)**	T_w / T_0
1	Stetson et al. (1984)[5]	7.99	2.5	1350	0.15 - 0.7	7	
2	Stetson et al. (1967)[3]	5.5	1.6 – 18.2	2020 to 2430	0.03125 - 0.5	8	
3	Stetson et al. (1983)[3]	6	9.7 – 30.3	1100	0.01 to 0.3	8	
4	Maslov et al. (2001)[9, 10]	6	3.5	707	0.0197-0.0295	7	
5	Muir et al. (1972)[23]	6	3.0 – 23.6	600	0.0025 - 0.8	8	
6	Stainback (1969)[24]	8	1.3 - 13	740 - 840	0 - 0.5	5	
7	Boudreau (1985)[25]	7	10 - 40	1000 - 1400	2.2	9.75	
8	Fischer (1970)[26]	6.9	1.68 – 6.26	1020 - 1280	0 – 0.6	10	0.45– 0.53
9	Horvath et al. (2002)[27]	6	0.5 - 8	300 – 540 (F)	0 – 0.0625	5	
10	Diaconis et al. (1957)[28]	3.12	2.25 - 8		0 – 0.1875		0.26
11	Rogers (1962)[29]	3.12 3.81	14 - 21	41 (C)	0 – 0.49	7.5	
12	Disher et al. (1956)[30]	8.17	18		0.4375	7.5	

2. Governing Equations and Numerical Methods

The governing equations for both steady and unsteady flow computations are briefly presented in this section. Details of the governing equations and numerical methods for two and three-dimensional flows have been described in previous papers[33-35]. The governing equations are the unsteady three-dimensional Navier-Stokes equations written in the following conservation-law form:

$$\frac{\partial U^*}{\partial t^*} + \frac{\partial F_j^*}{\partial x_j^*} + \frac{\partial F_{vj}^*}{\partial x_j^*} = 0 \tag{1}$$

where $U^* = (\rho^*, \rho^* u_1^*, \rho^* u_2^*, \rho^* u_3^*, e^*)$, and superscript "*" represents dimensional variables. The Cartesian coordinates, (x^*, y^*, z^*) , are represented by (x_1^*, x_2^*, x_3^*) in the tensor notation. In the current simulation of three-

dimensional flow over a blunt cone, x^* axis is along the center line of the axisymmetric cone pointing downstream. The origin of the Cartesian coordinate system is located at the center of the spherical nose cone.

For all results presented in this paper, unless specified otherwise, we nondimensionalize the flow velocities by the freestream velocity u_∞^*, length scales by the nose radius r_n^*, density by ρ_∞^*, pressure by p_∞^*, temperature by T_∞^*, time by r_n^* / u_∞^*, etc. The dimensionless flow variables are denoted by the same dimensional notation but without the superscript "*".

A 3-D fifth-order shock-fitting method of Zhong[33] is used to compute the flow field bounded by the bow shock and wall surface. In the discretization of the Navier-Stokes equations, spatial derivatives in the streamwise (s) and wall-normal (y_n) directions are modeled by a fifth-order finite difference schemes. The flow variables behind the shock are determined by the Rankine-Hugoniot relations across the shock and a characteristic compatibility equation from behind the shock. The details of the shock fitting formulas and numerical methods can be found in [33].

2 Flow Conditions

The flow conditions for the test case studied in this paper are the same as those in Stetson's experiments on air flow over a blunt cone in a Mach 5.5 freestream [3]. For the case of zero angle of attack, Stetson tested ten blunt cones of different nose radii ranging from 1/32 in to 1.5 in (see *Figure 1*). A range of different freestream unit Reynolds numbers were used to test these cones, from $1.6\times10^6 / ft$ to $18\times10^6 / ft$. In this paper, only three cases of different nose radii and a constant unit Reynolds number are used in the numerical simulation. The nose radii of the three cases are:

$$\begin{aligned} &\text{Case 1: } r_n = 1.5in = 38.1mm \\ &\text{Case 2: } r_n = 0.5in = 12.7mm \\ &\text{Case 3: } r_n = 0.15625in = 3.969mm \end{aligned} \tag{2}$$

All other flow conditions are the same for these three cases. The specific flow conditions are:

- $M_\infty = 5.468$
- $P_\infty^* = 7756.56\,Pa$, $T_\infty^* = 174.46K$
- Wall temperature: $T_w = 296K$
- $\gamma = 1.4$, $\mathrm{Pr} = 0.72$, $R^* = 286.94Nm/kgK$
- Freestream unit Reynolds number: $\mathrm{Re}_\infty^* = 18.95\times10^6 m^{-1}$
- Blunt cone half angle: $\theta = 8^\circ$, the freestream flow has a zero angle of attack
- Parameters in Sutherland's viscosity law: $T_r^* = 288K$, $T_s^* = 110.33K$, $\mu_r^* = 0.17894\times10^{-4} kg/ms$

where p_∞^* and T_∞^* are freestream pressure and temperature respectively. The body surface boundary condition is a non-slip condition for velocity and isothermal wall condition for temperature. In this particular study, both the steady base flow and unsteady flows are axisymmetric. The simulation is carried out by using 121 grid points between the cone surface and the shock (in the wall-normal direction). The simulation is carried out using many zones in the streamwise direction with 121 grid points per zone.

As stated earlier in this paper, the origin of the Cartesian coordinate system, (x, y, z), is located at the center of the nose of the spherical cone, where the x coordinate points from left to the right along the center line of the

axisymmetric cone. In addition to x, a natural coordinate s is also used in this paper and in [3] to measure the dimensionless curve length of a surface location starting from the stagnation point. The nondimensional s and x, which are normalized by the nose radius r_n, are related to each other by the following relation:

$$x = \begin{cases} -\cos(s) & (s \le 0.5\pi - \theta) \\ (s + \theta - \pi/2)\cos\theta - \sin\theta & (s > 0.5\pi - \theta) \end{cases} \tag{3}$$

where θ is the half angle of the cone. In the current test case, $\theta = 8^\circ$.

3 Nose Bluntness Effects on Steady Base Flow

The steady base flow solution of the three test cases of different nose bluntness stated in (2) has been obtained by using a fifth-order shock fitting scheme [33]. The mean flow solutions are also used for a concurrent linear stability analysis in [32]. In this paper, we will mainly present the effects of nose bluntness and the entropy layer on the steady flow field.

Figure 3 shows the Mach number contours for the three cases of steady base flow solution. The bow shock is obtained in the shock fitting simulation as the outer computational boundary of the contours. In all figures, unless marked with variable dimensions, the variables are dimensionless. The current figures show strong effects of the entropy layer near the nose region in Case 1 of the largest nose radius. Since flow properties undergo substantial changes passing through the bow shock, it is interesting to evaluate the local unit Reynolds numbers in the flow fields behind the bow shocks. The contours of the local unit Reynolds numbers of the three test cases are shown in *Figure 4*. By examining the contours, we can see that the cases of larger nose radii have thicker boundary layers and much lower local Reynolds numbers along the edge of the boundary layers.

The profiles of dimensionless pressure along the cone surface for the three test cases are shown in *Figure 5*. These profiles are typical of hypersonic flow over a blunt straight cone with a spherical nose. The maximum wall pressure is reached at the stagnation point. The surface pressure drops sharply as flow expands around the nose region. Because of the discontinuity in surface curvatures at the junction of the spherical nose and straight cone afterward, the flow experiences an over-expansion at the junction and goes through a recompression along the cone surface afterward. As a result, there is adverse pressure gradient along the surface locations after the junction. Further downstream, the surface pressure approaches a constant value. The region of this adverse pressure gradient is determined by the inviscid flow field behind the bow shock and can be scaled by the nose radius. As a result, the region is longer for the cases of larger nose radii.

Figure 6 shows the profiles of local Mach number, unit Reynolds number, and entropy immediately behind the bow shocks for the three sets steady base flows of different nose bluntness. The flow is subsonic in the stagnation region. The Mach number increases to a maximum value around 5 as s increases. The slight drop in Mach number for Case 3 at $s^* = 0.3m$ is caused by the expansion waves originated at the shoulder of the blunt nose. The effects of nose bluntness on the local Reynolds numbers and entropy at locations immediately behind the bow shock are significant.

It has been argued by many authors [3] that the cause of transition delay by slight nose bluntness is a result of the reduction of local Reynolds number at the edge of the boundary layer as the bluntness increases. For hypersonic flow over a blunt nose, the entropy layer behind the bow shock results in lower Mach numbers and local Reynolds numbers. If the local Reynolds number at transition remains a constant, the reduction of local Reynolds numbers leads to the downstream shift of the transition location. Stetson argued that when the nose bluntness is larger than a certain critical value, the local transitional Reynolds number decreases when nose bluntness increases further. This leads to transitional reversal. The mechanisms of reversal are still not understood.

Stetson used an approximate theory to show the distributions of Mach numbers and local unit Reynolds numbers at the edge of the boundary layers for three nose radii. The current numerical solutions can show exactly the effects of the entropy layer on the local properties at the edge of the boundary layers. The main effect of the entropy layer is

the reduction of local Reynolds numbers in the mean flow. *Figure 8* compares the profiles of local entropy, Mach numbers, local unit Reynolds numbers, local Reynolds numbers and temperatures along the edges of the boundary layers for the three cases of different nose radii. The dimensional natural coordinate s^* is used in the plots in order to compare the three cases of different nose radii. As r_n^* increases, the effect of entropy layer is stronger as shown by the reduction of edge Mach numbers. For the cases of larger nose radii, the edge entropy and temperature are higher. Most importantly, the local Reynolds numbers and unit Reynolds numbers along the edge of the boundary layers are much lower for the cases of larger nose radii. The only exception occurs in a small region immediate behind the spherical nose, where the local Reynolds number are higher of cases with larger r_n^*. This exception is not likely to be important because it happens in the region of very low Reynolds numbers. On the other hand, the increase of nose radii results in orders-of-magnitude smaller local Reynolds number downstream.

For this particular flow, the boundary layer is relatively thin compared to the stand-off distance between the bow shock and the cone surface as shown in *Figure* 9, which shows the profiles of local temperatures, tangential velocities, and $\rho(du_t / dy_n)$ along the wall normal direction located at $s^* = 0.5m$ for the three sets steady base flows of different nose bluntness. The figure shows that the variation of flow variables between the edge of the boundary layer and the bow shock is caused by the entropy layer behind the curved shock. *Figure 11* shows the profiles of local temperatures, tangential velocities, and $\rho(du_t / dy_n)$ along the wall normal direction at five grid stations along the cone surface for the steady base flows of Case 3 of $r_n^* = 0.15625in$. As s increases, the boundary layer becomes thicker and the effects of entropy layer decreases. It is interesting to note that, for the current cases, *Figure 9* and *Figure 11* show that there is no creation of generalized inflection point associated with the zero derivative of $\rho(du_t / dy_n)$.

4 Unsteady Flow Created by the Receptivity to Wall Blowing/Suction

As discussed in Introduction Section, the main objective of this paper is to study the transition reversal phenomenon reported in the Stetson's experiments [3] (*Figure 2*). Currently, the small bluntness effects of transition delay can be explained by the reduction of local Reynolds. The objectives of this paper and a companion paper [32] are to conduct the LST and DNS studies of the cases of Stetson's Mach 5.5 experiments on the nose bluntness effects. Since the LST results have been presented by [32], we will mainly focus on the DNS study of the instability of the boundary layers with different nose bluntness. Various aspects of the linear stability of the flow can be studied by numerical simulation of receptivity of the boundary layer to various disturbances. Examples of the external disturbances include freestream perturbations, surface roughness, surface blow and suction, surface vibrations, etc. The forcing disturbances can be both 2-D and 3-D disturbances. In this paper, we will present one test case of two-dimensional unsteady flow excited by wall blow and suction at fixed frequencies.

In the numerical simulation of the current paper, the instability waves in the boundary layer are induced by the blowing and suction imposed to a narrow strip of the cone surface. Even though the nonlinear Navier-Stokes equations are used in the simulation, the amplitudes of the forcing waves are chosen to be weak enough so that the disturbances excited in the boundary layer are in the linear regime. In doing so, the growth rates obtained from the simulation can be directly compared with those of the linear growth rates computed by LST. In the unsteady flow simulation, we introduce forcing disturbances of a mixture of 15 frequencies. The range of frequencies for each nose radius is determined by the corresponding LST analysis. The subsequent receptivity and development of the instability waves at these frequencies are computed by the numerical simulation. The surface blowing and suction is applied by specifying perturbations to the wall normal velocities in the following form,

$$v_{n,wall}(x,t) = \varepsilon \sin\left[\alpha_w (x - x_0)\right] \sum_{n=1}^{N} A_n \cos(\omega_n t + \phi_n) \qquad (x_0 < x < x_1) \tag{4}$$

where ε represents the forcing disturbance amplitude. The specific forcing waves introduced by the blowing and suction are a mixture of $N = 15$ independent frequencies, i.e.,

$$f_n^* = n f_1^* \qquad (n = 1, 2, \cdots, N) \tag{5}$$

Figure 10 shows the dimensional growth rates of the second mode, computed by Lei and Zhong [32], for Case 3 of the current paper. Since the current unsteady simulation is limited to the region between $s^* = 0.1m$ and $s^* = 0.3m$, the lowest frequency for this case is chosen to be:

$$\text{Case 1: } r_n = 1.5in,\ f_1^* = 17517.0Hz \tag{6}$$

The remaining 14 frequencies are multiples of f_1^* given by Eq. (5). The highest frequencies for the unsteady simulation is $f_{15}^* = 262754.3Hz$, which corresponds to one of the frequencies shown in *Figure 10*.

Since the purpose of the current study is to study the linear stability of the boundary layer, ε is chosen to be small enough so that the boundary-layer response to the forcing disturbances is linear. Hence, in the current simulation, the overall forcing wave amplitude is chosen to be

$$\varepsilon = 10^{-5} \tag{7}$$

which is small enough that the receptivity process falls in the linear regime. The wave components of the 15 frequencies are independent, and they can be decomposed one from another by a temporal Fourier analysis. In addition, because the forcing waves are linear, the use of normal velocity perturbations on the surface does not introduce net mass flux into the flow. Since the wave components of different frequencies are linearly independent, the phase angles ϕ_n of the forcing waves at frequency ω_n are chosen randomly. The 15 sets of wave frequencies, relative forcing amplitudes A_n for all frequencies are set to be unity in this study.

Figure *11* shows the contours of temperature and velocity perturbations for unsteady flow for the frequency of $f_{15}^* = 262.754kHz$ for Case 1 of nose radius of 1.5 *in*. The blow-suction slots are located approximately at $s^* = 0.1m$. The contours show the growth of instability as the perturbations waves travel downstream. The growth can be seen more clearly in *Figure 12*, which shows the distribution of the real part of tangential velocity perturbations along the cone surface for unsteady flow at the same frequency. Since the simulations are carried out by a multi-zonal approach, the distribution contains gaps in zonal boundaries. Never the less, the growth of the instability wave induced by the forcing waves are evident.

Figure 13 shows the distribution of amplitudes of pressure perturbations along the cone surface for unsteady flow with fifteen frequencies ($f_n = n \times 17.517kHz$) in Case 1. For higher frequencies in the range of f_7 to f_{15}, a clear instability wave emerges after the initial transient induced by the forcing waves. For frequencies lower than f_7, the flow is stable in the simulation and the solutions contains strong initial transients. Based on the results of this figure, the growth rates of the perturbations can be computed according to the following formula:

$$\alpha_i = \frac{d\,|\,p\,|}{ds^*}\frac{1}{|\,p\,|} \tag{8}$$

where $|\,p\,|$ is the amplitude of surface pressure perturbations obtained by a temporal Fourier analysis of the instantaneous pressure. *Figure* 14 shows the distribution of dimensional growth rates along the cone surface for the nine higher frequencies of $f_n = n \times 17.517kHz$ where $n = 7,8,\cdots,15$. For the frequency of $f_{15}^* = 262754.3Hz$, this figure shows that the maximum growth rate is around $18.5/m$, which is very close to the peak LST growth rate of the same frequency shown in *Figure 10*. On the other hand, the growth region for this frequency along the surface predicted by LST is narrower than those shown by the numerical simulation. The differences may be due to the strong nonparallel effects in Case 1 at s^* around 0.15m. As shown by *Figure 3* and *Figure 4*, the flow field of Case 1 in this region is very closed to the nose region and flow can be highly nonparallel.

Work is on-going to simulate and compare the instability wave fields for the three test cases of different nose radii. The effects of nose bluntness on the instability will be studied by numerical simulation of the unsteady flow fields. The results will be reported in future papers. Meanwhile, LST computations of the three cases in [32] do not show the reversal effects in second mode instability waves in for the case of very large nose radii.

5 Conclusions

A numerical simulation study has been conducted on the mean flow and the receptivity of Mach 5.5 hypersonic flow over a blunt cone due to surface blow and suction. The flow conditions are those of Stetson's 1967 wind-tunnel experiments for Mach 5.5 flow over a 8° half-angle blunt cone. These experiments are among the very few cases showing transition reversal due to nose bluntness. In this paper, three nose radii of 0.0156in, 0.5in, and 1.5in are used to study the mechanisms of the transition reversal. The simulation results show that the increase of nose bluntness leads to the substantial decrease in local Reynolds numbers along the edge of the boundary layers. The decrease of local Reynolds numbers is the main reason of transition delay by nose blunting in the small nose bluntness region. On the other hand, the cause of transition reversal in large nose bluntness regime is still not clear. We have finished one case of unsteady flow of boundary layer instability induced by surface blow and suction. The results show growth of second mode instability in the boundary layer. The maximum second mode growth rates computed by the unsteady flow simulation agree well with those of LST calculation by Lei and Zhong [32]. More extensive unsteady flow computations will be carried out to investigate the nose bluntness effects and transition reversal by direct numerical simulation.

Acknowledgments

This work was sponsored by the Air Force Office of Scientific Research, USAF, under AFOSR Grant #FA9550-07-1-0414, monitored by Dr. John Schmisseur. The views and conclusions contained herein are those of the author and should not be interpreted as necessarily representing the official policies or endorsements either expressed or implied, of the Air Force Office of Scientific Research or the U.S. Government.

References

1. Schneider, S.P., *Hypersonic Laminar-Turbulent Transition on Circular Cones and Scramjet Forebodies.* Progress in Aerospace Sciences, 2004. 40: p. 1-50.
2. Schneider, S.P., *Flight Data for Boundary-Layer Transition at Hypersonic and Supersonic Speeds.* Journal of Spacecraft and Rockets, 1999. 36(1): p. 8-20.
3. Stetson, K.F., Rushton, G. H., *Shock Tunnel Investigation of Boundary-Layer Transition at M = 5.5.* AIAA JOURNAL, 1967. 5(5): p. 899-906.
4. Ericsson, L.E., *Effects of Nose Bluntness and Cone Angle on Slender Vehicle Transition.* AIAA Paper 87-1415, 1987.
5. Stetson, K.F., Thompson, E. R., Donaldson, J. C., and Siler, L. G., *Laminar Boundary Layer Stability Experiments on a Cone at Mach 8, Part 2: Blunt Cone.* 1984. AIAA paper 84-0006.
6. Stetson, K.F.a.K., R., *On the Breakdown of a Hypersonic Laminar Boundary Layer*. 1993. AIAA Paper 93-0896.
7. Demetriades, A., *Hypersonic Viscous Flow Over A Slander Cone. Part III: Laminar Instability and Transition.* AIAA paper 74-535, 1974.
8. Demetriades, A., *Laminar Boundary Layer Stability Measurements at Mach 7 Including Wall Temperature Effects.* AFOSR-TR-77-1311, 1977.
9. Maslov, A.A., Shiplyuk, A. N., Sidorenko, A., and Arnal, D., *Leading-edge Receptivity of a Hypersonic Boundary Layer on a Flat Plate.* Journal of Fluid Mechanics, 2001. 426: p. 73-94.
10. Maslov, A.A., Mironov, S. G., Shiplyuuk, A. A., Sidorenko, A. A., Buntin, D. A., and Aniskin, V. M., *Hypersonic Flow Stability Experiments.* 2002. AIAA 2002-0153.
11. Malik, M.R., Spall, R. E., and Chang, C. L., *Effect of Nose Bluntness on Boundary Layer Stability and Transition.* 1990. AIAA Paper 90-0112.
12. Herbert, T.a.E., V., *Stability of Hypersonic Flow over a Blunt Body.* AGARD CP, 1993. 514: p. 28.
13. Kufner, E., Dallmann, U., and Stilla, J., *Instability of Hypersonic Flow Past Blunt Cones - Effects of Mean Flow Variations.* 1993. AIAA paper 93-2983.

14. Kufner, E., and Dallmann, U. *Entropy and Boundary Layer Instabilityof Hypersonic Cone Flows - Effects of Mean Flow Variations*. in *IUTAM Symposium on Laminar-Turbulent Transition*. 1994. Sendai/Japan: Springer-Verlag, Berlin.
15. Rosenboom, I., Hein, S., and Dallmann, U., *Influence of Nose Bluntness on Boundary-Layer Instabilities in Hypersonic Cone Flows* AIAA Paper 99-3591, 1999.
16. Potter, J.L., and Whitfield, J. D. *Boundary-Layer Transition under Hypersonic Conditions*. in *Recent Developments in Boundary Layer Research, Part III*. 1965.
17. Zhong, X., *Numerical Simulation and Experimental Comparison of Hypersonic Boundary Layer Instability over a Blunt Cone.* AIAA paper 2004-2244, 2004.
18. Zhong, X., and Ma, Y., *Boundary-layer receptivity of Mach 7.99 Flow over a blunt cone to free-stream acoustic waves.* Journal of Fluid Mechanics, 2005. 556: p. 55-103.
19. Zhong, X., *Effect of Nose Bluntness on Hypersonic Boundary Layer Receptivity over a Blunt Cone.* AIAA paper 2005-5022, 2005.
20. Esfahanian, V., *Computation and stability analysis of laminar flow over a blunt cone in hypersonic flow*. 1991, The Ohio State University.
21. Stetson, K.F., *Nosetip Bluntness Effects on Cone Frustum Boundary Layer Transition in Hypersonic Flow.* AIAA paper 1983-1763, 1983.
22. Softley, E.J., *Transition of the Hypersonic Boundary Layer on a Cone: Part II - Experiments at Mach 10 and More on Blunt Cone Transition*, in *GE Space Science Lab, R68SD14*. 1968.
23. Muir, J.F., Trujillo, A. A., *Experimental investigation of the effects of nose bluntness, freestream Reynolds number, and angle of attack on cone boundary layer transition at a Mach number of 6.* AIAA Paper 72-216, 1972.
24. Stainback, P.C., *EFFECT OF UNIT REYNOLDS NUMBER, NOSE BLUNTNESS, ANGLE OF ATTACK, AND ROUGHNESS ON TRANSITION ON A 5" HALF-ANGLE CONE AT MACH 8.* NASA TN D-4916, 1969: p. 1-79.
25. Boudreau, A.H., *Transition measurements via heat-transfer instrumentation on a 0.5 bluntness 9.75-deg. cone at Mach 7 with and without mass addition.* AIAA Paper 85-1004, 1985: p. 1-7.
26. Fischer, M.C., *An experimental investigation of boundary-layer transition on a 10-deg. half-angle cone at Mach 6.9.* Technical Report NASA TN-D-5766, 1970: p. 1-63.
27. Horvath, T.J., Berry, S. A., Hollis, B. R., Chang, C.-L., Singer, B. A., *Boundary layer transition on slender cones in conventional and low disturbance Mach 6 wind tunnels.* AIAA Paper 2002-2743, 2002: p. 1-23.
28. Diaconis, N.S., Jack, J. R., Wisniewski, R. J., *Boundary-Layer Transition at Mach 3.12 as Affected by Cooling and Nose Blunting.* NACA TN-3928, 1957: p. 1-17.
29. Rogers, R.H., *The Effect of Tip Bluntness on Boundary-Layer Transition on a 15 Deg Included Angle Cone at M = 3.12 and 3.81*. MINISTRY OF AVIATION AERONAUKAl RESEARCU COUNCIL CURRENT PAPERS, 1962. C.P. No. 598: p. 1-44.
30. Disher, J.H., Rabb, L., *Observation of Laminar Flow on a Blunted 15 Deg Cone-Cylinder in Free Flight at High Reynolds Numbers and Free-Stream Mach Number to 8.17.* NACA RM E56G23, 1956: p. 1-33.
31. Stetson, K.F., Thompson, E. R., Donaldson, J. C., and Siler, L. G., *Laminar Boundary Layer Stability Experiments on a Cone at Mach 8, Part 4: On Unit Reynolds Number and Environmental Effects.* 1986. AIAA Paper 86-1087.
32. Lei, J., and Zhong, X., *Linear Stability study of Hypersonic Boundary Layer Transition on Blunt Circular Cones* AIAA Paper 2009-0939, 2009.
33. Zhong, X., *High-Order Finite-Difference Schemes for Numerical Simulation of Hypersonic Boundary-Layer Transition.* Journal of Computational Physics, 1998. 144: p. 662-709.
34. Zhong, X., *Leading-Edge Receptivity to Free Stream Disturbance Waves for Hypersonic Flow over a Parabola.* Journal of Fluid Mechanics, 2001. 441: p. 315-367.
35. Zhong, X., *Additive Semi-Implicit Runge-Kutta Schemes for Computing High-Speed Nonequilibrium Reactive Flows.* Journal of Computational Physics, 1996. 128: p. 19-31.

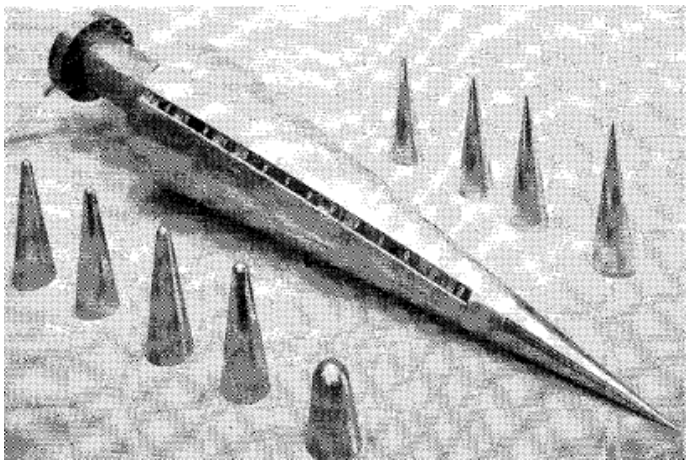

Figure 1. Sharp and blunt cone models with an 8 degree half angle used in Stetson's transition experiments in a Mach 5.5 shock tunnel [3].

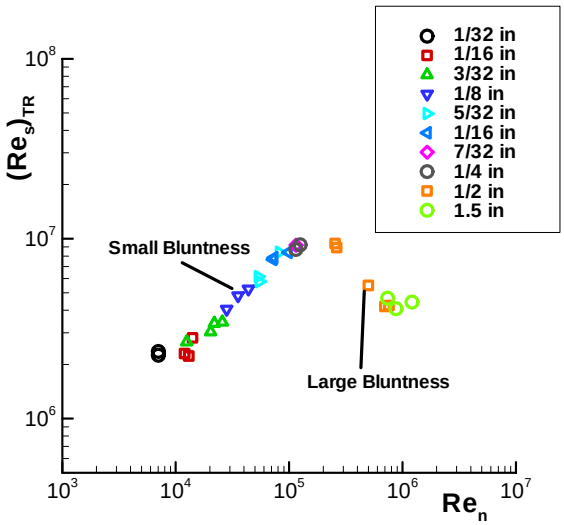

Figure 2. Transitional Reynolds numbers vs. nose radius Reynolds numbers, based on freestream flow conditions, for Stetson's Mach 5.5 experiments (from Table 2 of [3]). The legends specify the nose radii of the test cases.

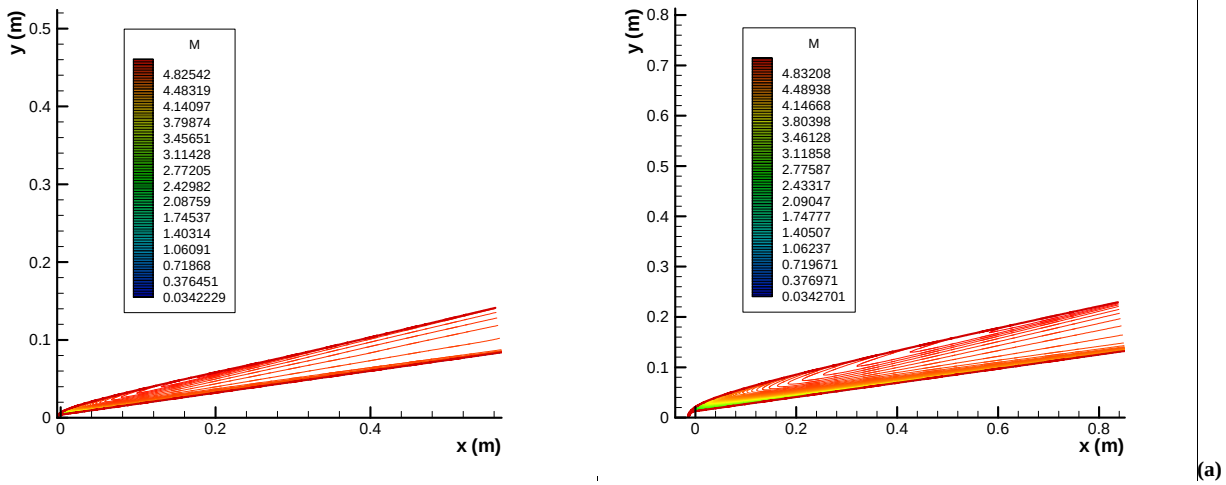

(Case 3: : $r_n = 0.156in$ **)** **(Case 2: :** $r_n = 0.5in$ **)**

(a)

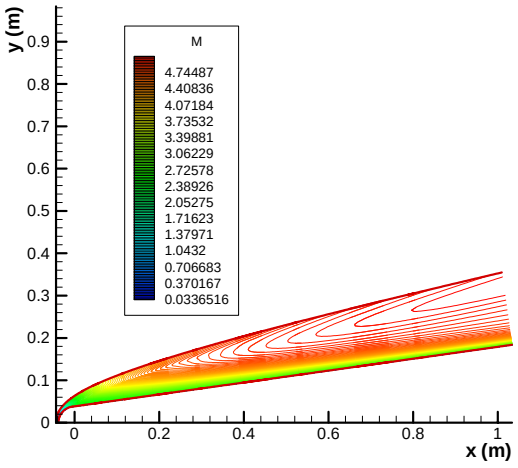

(Case 1: $r_n = 1.5in$ **)**

Figure 3. Mach number contours of the three test cases of different nose radii.

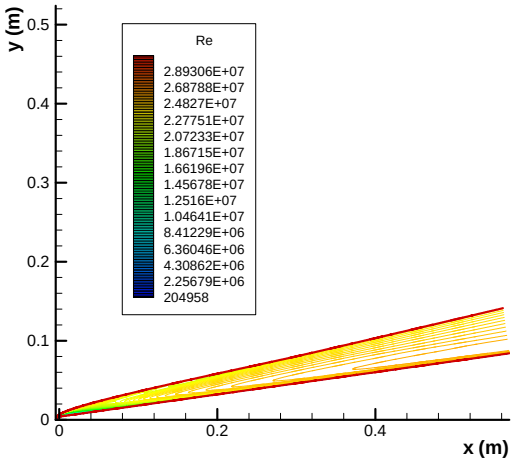

(Case 3: : $r_n = 0.156in$ **)**

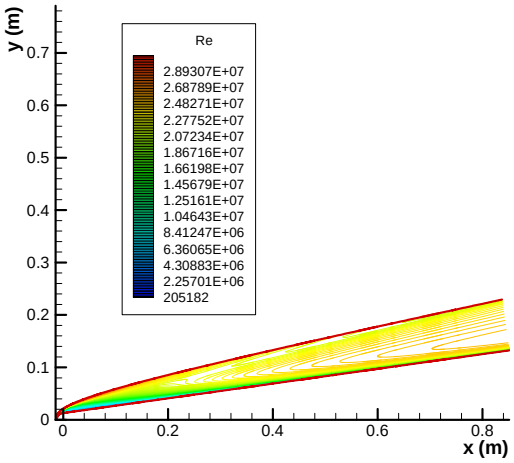

(Case 2: : $r_n = 0.5in$ **)**

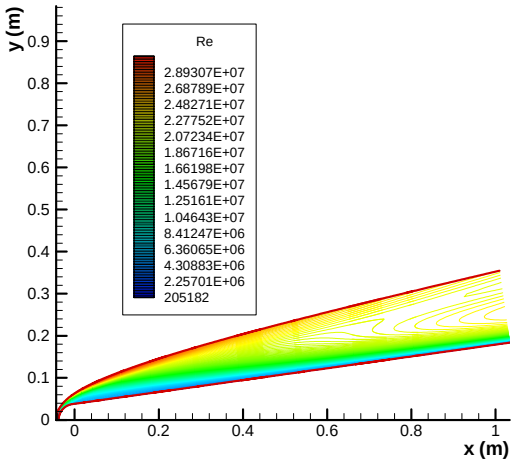

(Case 1: $r_n = 1.5in$ **)**

Figure 4. Local unit Reynolds number contours of the three test cases of different nose radii.

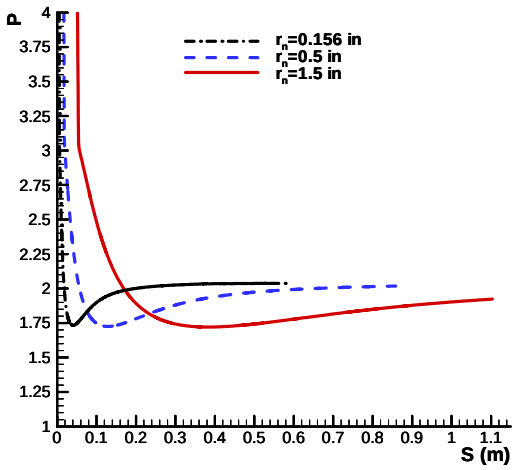

Figure 5. Pressure distributions along the cone surfaces for the three sets steady base flows of different nose bluntness.

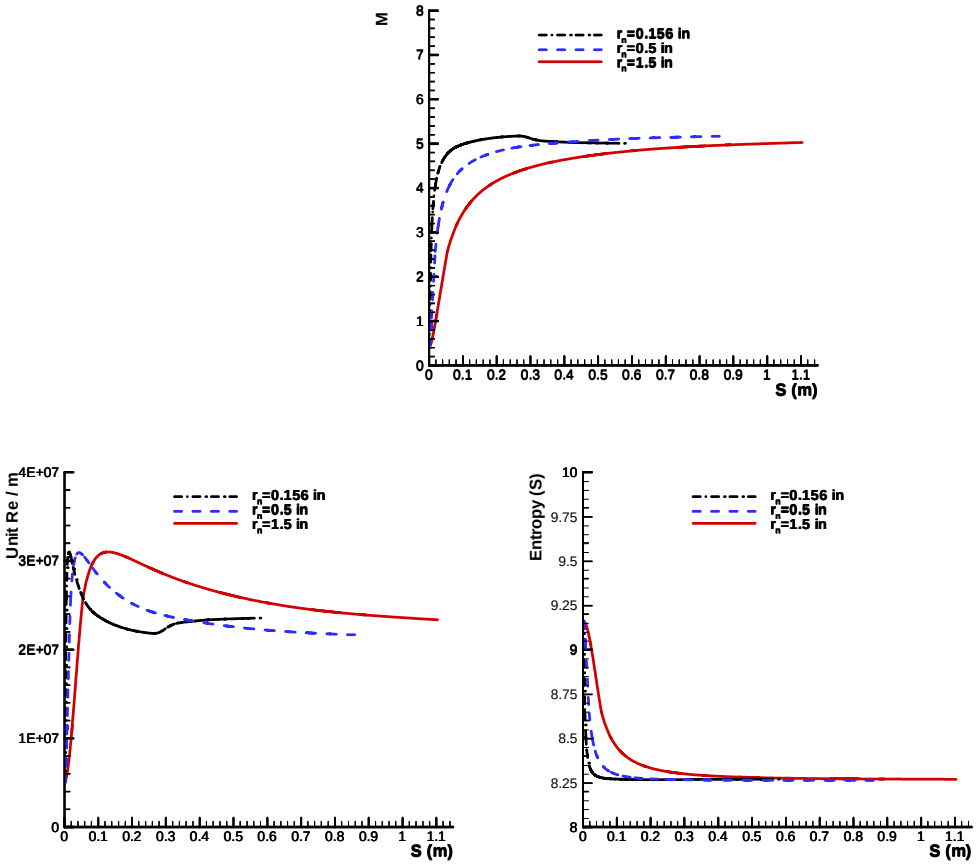

Figure 6. Profiles of local Mach numbers, unit Reynolds numbers, and local Reynolds numbers immediately behind the bow shock for the three sets steady base flows of different nose bluntness.

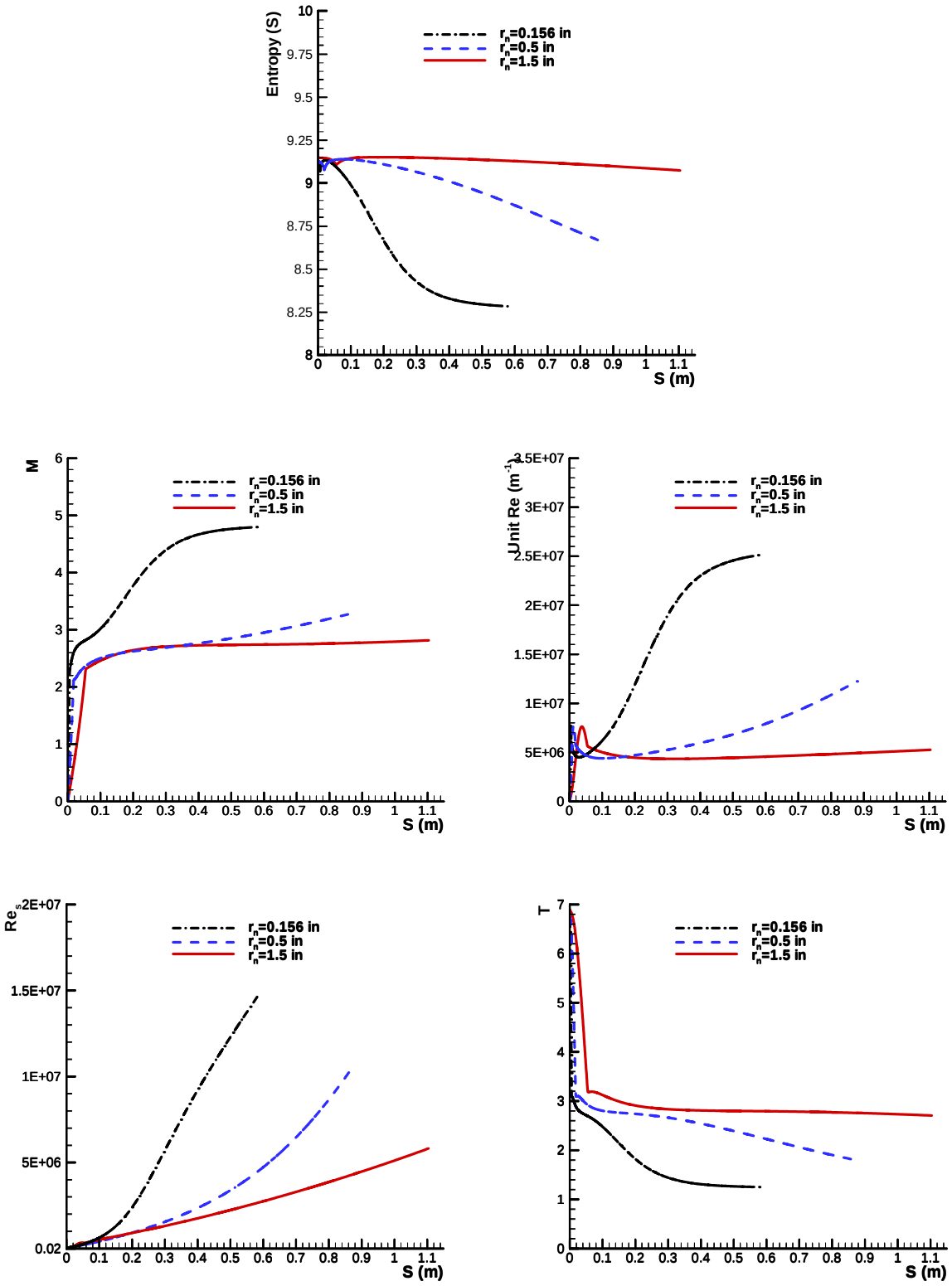

Figure 7. Profiles of local Mach numbers, temperatures, entroy, unit Reynolds numbers, and local Reynolds numbers along the edges of boundary layers for the three sets steady base flows of different nose bluntness.

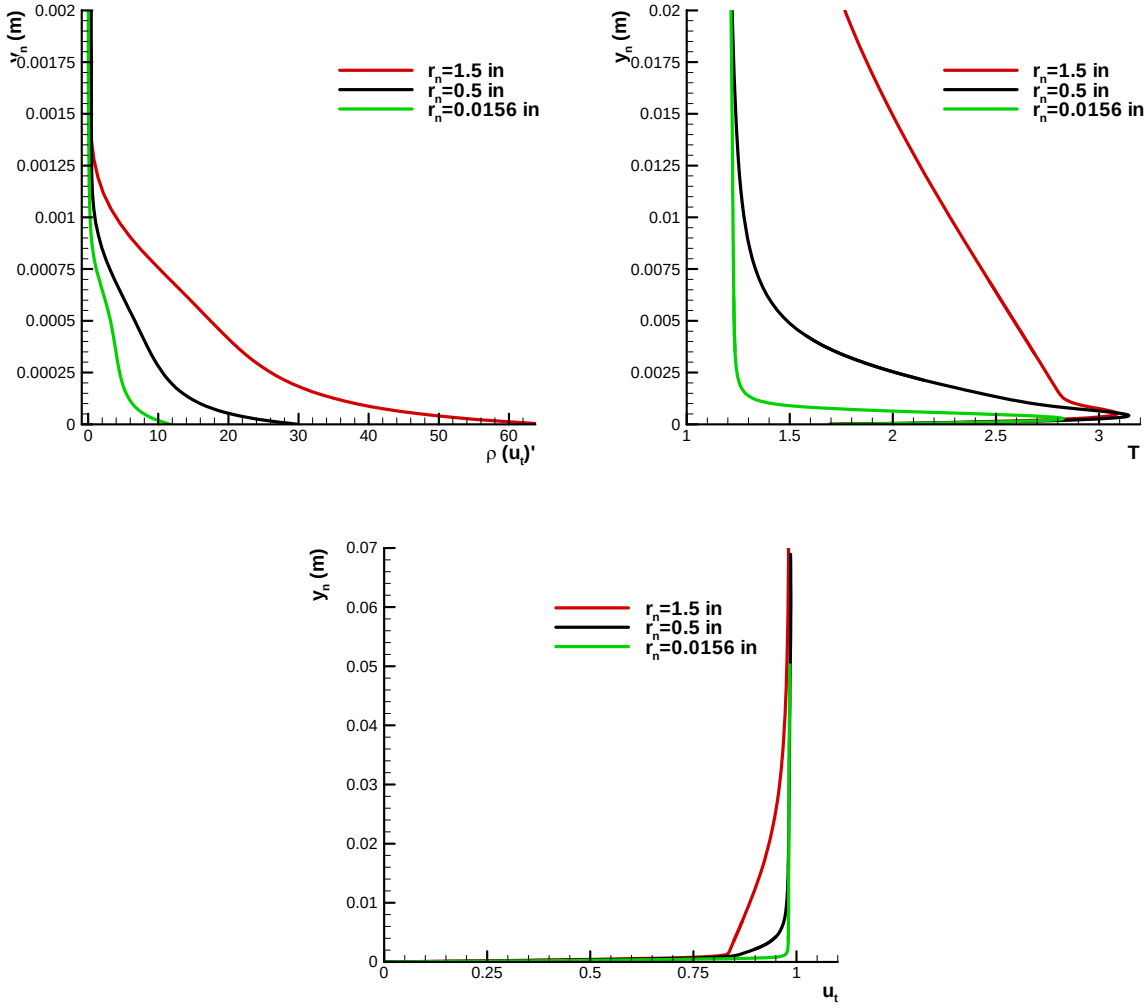

Figure 8. Profiles of local temperatures, tangential velocities, and $\rho(du_t / dy_n)$ ***along the wall normal direction located at*** $s = 0.5m$ ***for the three sets steady base flows of different nose bluntness.***

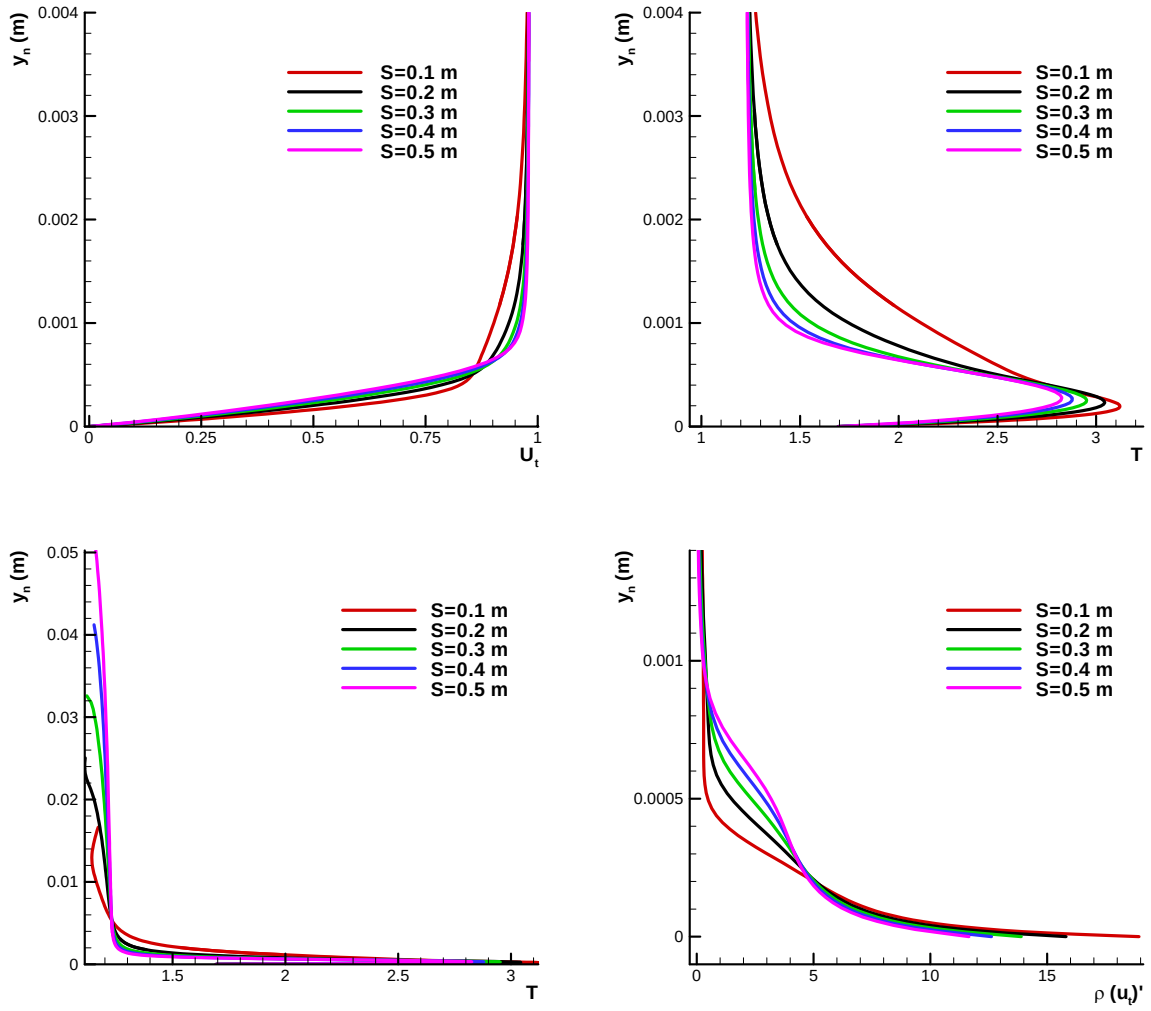

Figure 9. Profiles of local temperatures, tangential velocities, and $\rho(du_t/dy_n)$ along the wall normal direction at five grid stations along the cone surface for the steady base flows of Case 3.

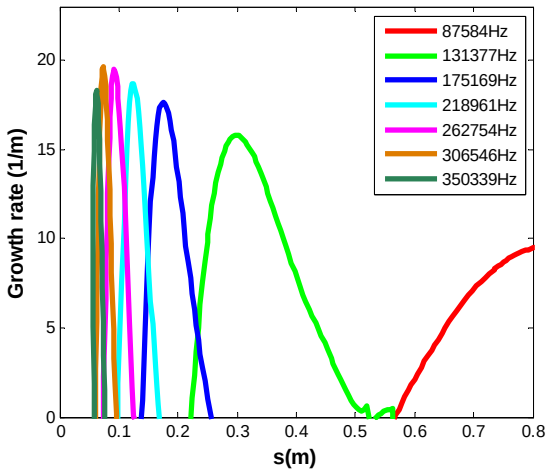

Figure 10. Second-mode dimensional growth rates, computed by Lei and Zhong [32], for Case 1 of the current paper.

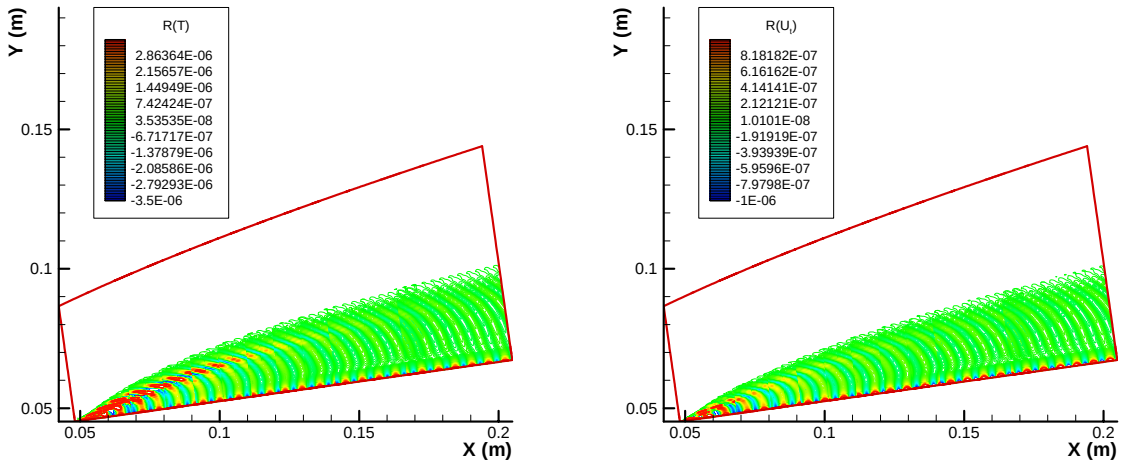

Figure 11. Contours of temperature and velocity perturbations for unsteady flow with $f_{15}^{*} = 262.754kHz$ ***for Case 1 of nose radius of 1.5 in.***

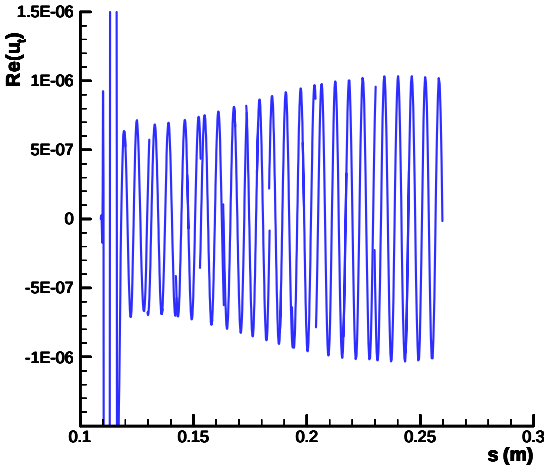

Figure 12. Distribution of the real part of tangential velocity perturbations along the cone surface for unsteady flow with $f_{15}^{*} = 262.754kHz$ ***for Case 1 of nose radius of 1.5 in.***

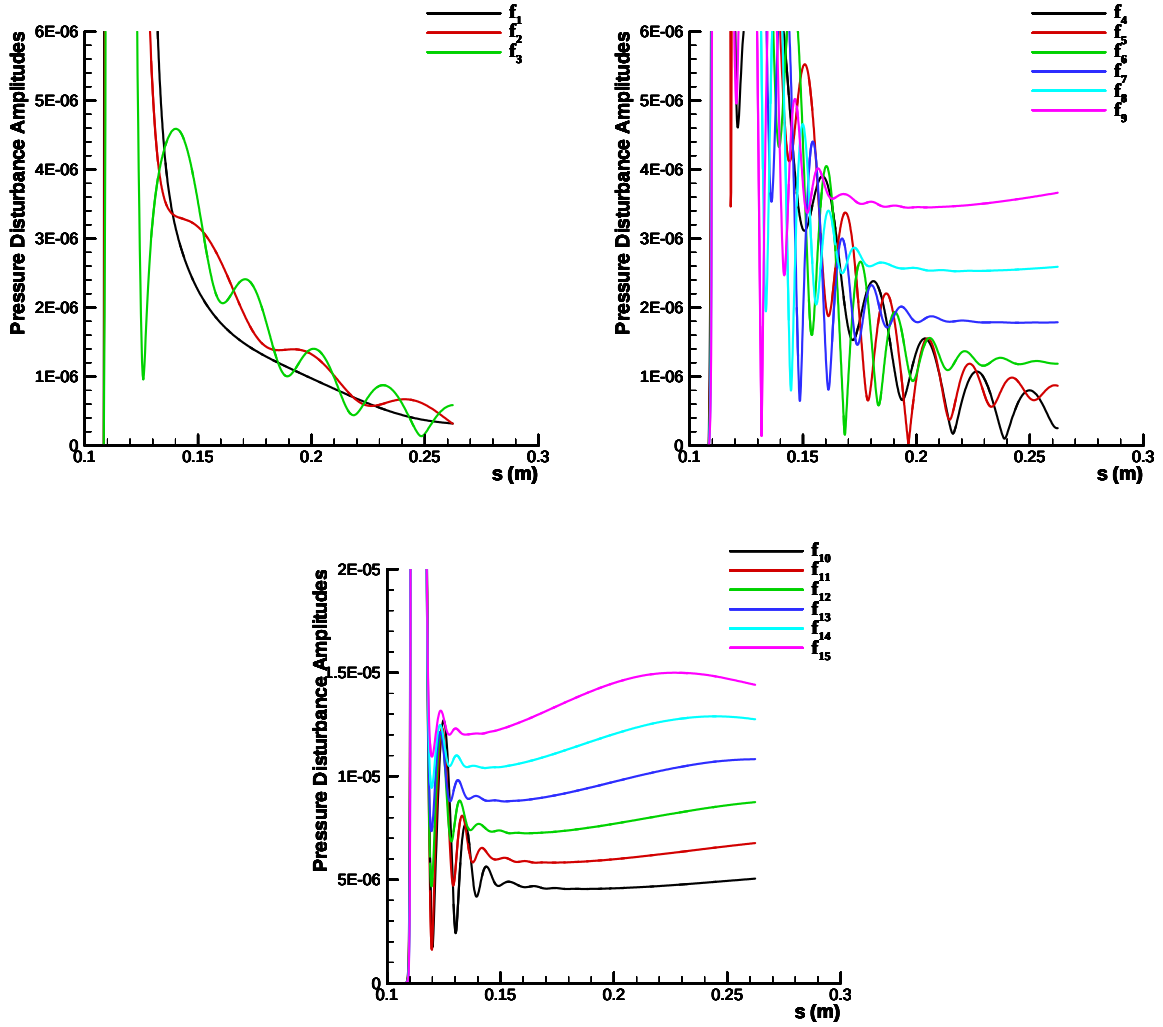

Figure 13.Distribution of the amplitudes of pressure perturbations along the cone surface for unsteady flow with fifteen frequencies ($f_n = n \times 17.517 kHz$) in unsteady flow with nose radius of 1.5 in.

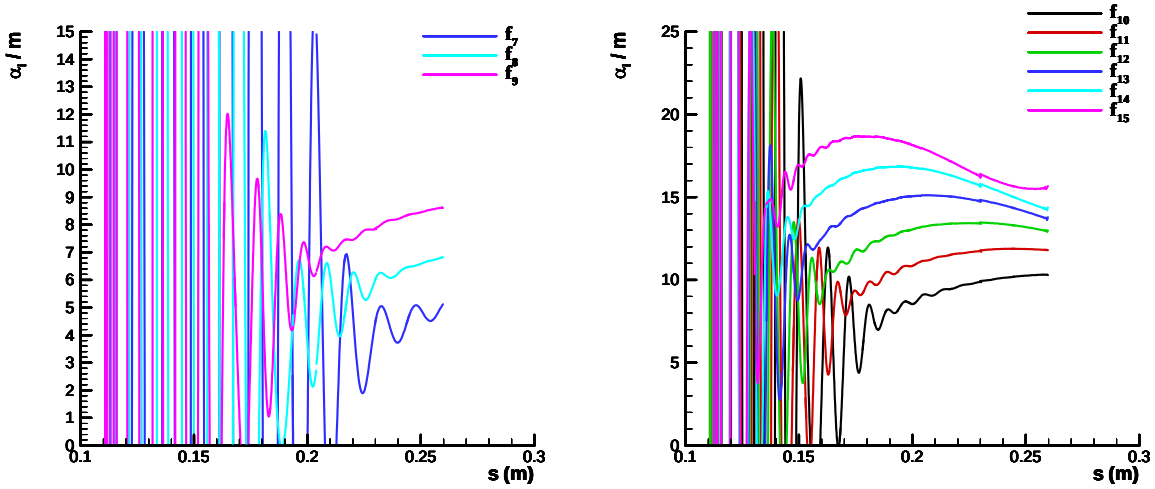

Figure 14.Distribution of dimensional growth rates along the cone surface for unsteady flow with nine frequencies ($f_n = n \times 17.517 kHz$) in unsteady flow with nose radius of 1.5 in.